

## Effect of Lattice Structure and Composite Precursor on Mechanical Properties of 3D-Printed Bone Scaffolds

M. Shams<sup>1,2\*</sup>, Z. Mansurov<sup>1,2</sup>, C. Daulbayev<sup>1,2</sup>, B. Bakbolat<sup>1,2</sup>

<sup>1</sup>al-Farabi Kazakh National University, 71 Al-Farabi ave., Almaty, Kazakhstan

<sup>2</sup>Institute of Combustion Problems, 172 Bogenbay batyr str., Almaty, Kazakhstan

### Article info

*Received:*  
8 April 2021

*Received in revised form:*  
5 June 2021

*Accepted:*  
17 August 2021

### Keywords:

Bone Scaffolds  
3D printing  
Hydroxyapatite  
Stereolithography  
Calcium pyrophosphate  
Bioscaffold

### Abstract

This article presents an investigation on designing and fabricating scaffolds with different structures, desired porosity, composition, and surface area to volume ratio (SA:V) for orthopedic applications by using the computer-aided design (CAD) and the stereolithography (SLA) 3D printing technique. Different triply periodic minimal surfaces (TPMS) and functionally graded lattice structures (FGLS) were designed based on various cell geometries. Finite element analysis (FEA), tensile and compression tests were carried out, and the results are presented. Two different resin compositions were used to print the models and compare the effect of resin precursors on the mechanical properties of scaffolds. The first was a biodegradable resin made from soybean oil commercially available on the market (made by Anycubic Co.). The second was a mixture of biodegradable UV-cured resin with 5% W/W of hydroxyapatite (HA) and 5% W/W calcium pyrophosphate (CPP). Bio-Hydroxyapatite and Bio-Calcium Pyrophosphate were obtained from eggshells waste and characterized using XRD and FESEM. The obtained data show that adding resin precursors (HA/CPP) slightly decreases the mechanical strength of printed scaffolds; however, considering their extraordinary effect on bone regeneration, this small effect can be ignored, and HA/CPP can be used as an ideal agent in bioscaffolds.

## 1. Introduction

In the 21<sup>st</sup> century, 3D-Printing is poised to play a fundamental role in the personalized regenerative medicine field. It has slowly evolved to create bio-screws, implants, and scaffolds for tissue engineering limited by the diversity of biomaterials that are usable in this field. Recently, many efforts have been made to develop and manufacture novel biomaterials and compositions to use in additive manufacturing [1].

Some of the most important advantages of manufacturing scaffolds using three-dimensional printing are Low cost of production, good control on porosities, co-culture of multiple cells, flexible and accurate personalization tailored to the target area, and the ability to create complex geometries [2].

\*Corresponding author.  
E-mail: shams.m.iau@gmail.com

The body's ability to repair damaged parts is limited by factors such as tissue type and the need for growth hormones (severe injuries). Any defect beyond this critical size needs external support, and these supports are called scaffolds. Two crucial factors shape the use of scaffolds: the type of biomaterial and the fabrication procedure [3, 4].

Traditional engineering designs are based on isotropic materials, which in most cases are less challenging to manufacture, simulate, and procure. The difference between scaffolds made by 3D printers and traditional methods like using molds is that in additive manufacturing, the shapes include user-defined infill geometries, which replace the solid internal volume with a structural lattice known as infill. The most significant effect of infill shape is on mechanical properties such as strength, toughness, hardness, stiffness, hardenability, brittleness, malleability, ductility, resilience, creep, slip, etc. [5, 6].

From the structural point of view, a scaffold should have a porous structure of appropriate interconnected pore networks and proper pore size for efficient mass-transport activities, including nourishment of cells, oxygen, exchange of nutrients, and cell migration [7]. Various tests confirm more cellular activity in the porous scaffolds than in the massive ones [8]. The Cells can immigrate to the site of action using the platform made by scaffolds and form new tissue. Consequently, scaffolds play a crucial role in tissue engineering and regenerative medicine. Loading the scaffolds with growth factors accelerates cells' differentiation to preferred lineage types to assist new tissue formation.

The lightweight of a scaffold is a great advantage for medical uses. According to the defined computer-aided design, standard infill percentages are 10 to 25%, which means a scaffold with an infill structure can be printed much faster than a solid scaffold. Furthermore, from an industrial point of view, production costs will reduce as less material is required to produce the object.

Personalized scaffolds can be designed according to specific and individual defects of each patient by converting the two-dimensional images obtained from the computerized tomography (CT scan) and magnetic resonance imaging (MRI) to 3D models, which can be modified in CAD software.

The thigh bone (The Femur) is the proximal bone of the hindlimb in tetrapod vertebrates. According to experiments, both femurs are the most robust and longest body bones [9]. Mechanical strength tests and finite element analysis of 3D printed scaffolds were performed to provide technical and academic communities with a new approach to improving mechanical and digital design in additive manufacturing, specifically stereolithography.

In addition to affecting the mechanical properties [10, 11], the infill geometry and percentage also affect drug release from 3D printed scaffolds [12].

We used Grasshopper 3D, which is a visual programming language to design infill patterns by parametric modeling. In parametric modeling, the scaffolds are modeled using pre-defined parameters. There is no need to design from scratch for each person individually; therefore, created models can be customized and personalized easily for other patients according to the bone defect and shape.

The pores size in all models was determined to be between 100 to 500  $\mu\text{m}$  which is the optimum size reported in previous investigations [13].

Hydroxyapatite is the mineral constituents of human bone and teeth that belong to the apatite group with a general chemical formula of  $\text{M}_{10}(\text{XO}_4)_6\text{Z}_2$ , in which  $\text{M} = \text{Ba}^{2+}, \text{Ca}^{2+}, \text{Sr}^{2+}, \text{Pb}^{2+}, \text{Na}^+, \text{La}^{3+}$ ;  $\text{XO} = \text{VO}_4^{3-}, \text{AsO}_4^{3-}, \text{PO}_4^{3-}, \text{CO}_3^{2-}$ ;  $\text{Z} = \text{Cl}^-; \text{OH}^-, \text{F}^-; \text{CO}_3^{2-}$  [14]. HA includes the greatest similarity with the biominerals' function and structure, such as teeth and bone, making it significant for researchers treating dental and bone defects [15]. HA and CPP's Nontoxicity, biocompatibility, bioactivity, bioaffinity, osteointegration, osteoconduction, and osteoinduction properties have made them the major candidates as an artificial bone substitute in modern orthopedic surgery and biomedical engineering [16–18].

This study investigates the effect of design/structure and resin composite precursors (HA, CPP) on the mechanical properties (Tensile and Compression) of the 3D printed scaffolds. Different lattice structures (inspired by mathematical models) were designed and printed by stereolithography 3D printing using biodegradable resin, hydroxyapatite, and calcium pyrophosphate composite. No previous study has been found on the effect of using HA/ CPP as resin reinforcement precursors on the mechanical properties of printed scaffolds, and this study can be used as a basis for further research. Considering HA/ CPP directly affects the stimulating bone regeneration rate, this composition can be used to find a balance between mechanical properties and the bioactivity of scaffolds. Results of mechanical tests are presented.

## 2. Material and methods

All chemicals used in this study were supplied by the MilliporeSigma company and used without further purification. The X-ray diffraction analysis was used to examine the crystal phase of the synthesized HA and CPP powders. Field emission scanning electron microscopy was used to visualize the morphology of powders. The displacement method (submersion) was used to calculate the porosity and density of scaffolds.

### 2.1. HA and CPP synthesis

Biodegradable hydroxyapatite and calcium pyrophosphate were obtained from eggshells waste [19, 20]. Produced powders were placed in a furnace at 1000  $^{\circ}\text{C}$  for 5 h to perform heat treatment [21] then ground for 1 h by planetary ball mill. Scherrer's equation used to calculate the average crystallite size of the HA and CPP particles as below:

$$\tau = \frac{K\lambda}{\beta \cos \theta}$$

where:  $\tau$  is the mean size of the ordered (crystal-line) domains;  $K$  is a dimensionless shape factor;  $\lambda$  is the X-ray wavelength;  $\beta$  is the line broadening at half the maximum intensity;  $\theta$  is the Bragg angle.

## 2.2. Designing scaffolds

Scaffolds were modeled using Rhino 7 and Transforming to a polygon mesh, and preparation

for 3D printing was done by Autodesk Meshmixer. 3D Slicer 4.11 was used to convert 2D computed tomography images to a 3D model, and optimization for use in Abaqus was done by Altair HyperMesh 2020. The CT Scan of the femur bone of a 37 years old patient was received in collaboration with SEMA hospital (Almaty, Kazakhstan) and used as a bone defect model (Fig. 1).

TPMS and FGLS structures were designed based on various cell geometries. Figure 2 shows the parametric design steps of a honeycomb scaffold from the elementary cell geometry using the grasshopper plugin in Rhino 7.

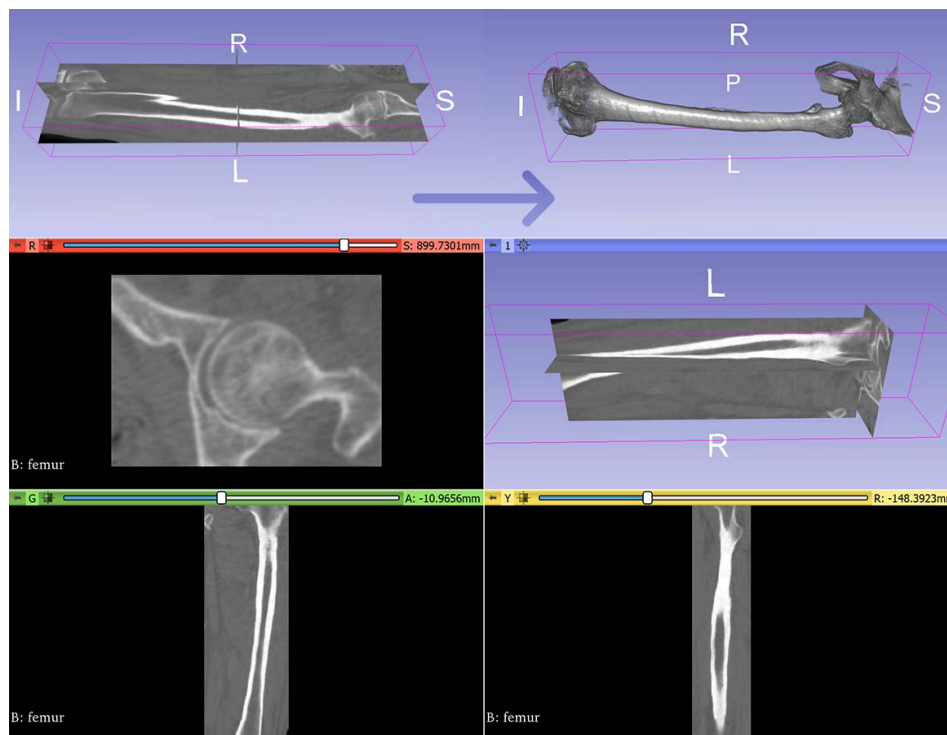


Fig. 1. Transforming the 2D computed tomography images of the Femur bone to a 3D model using 3D Slicer 4.11.

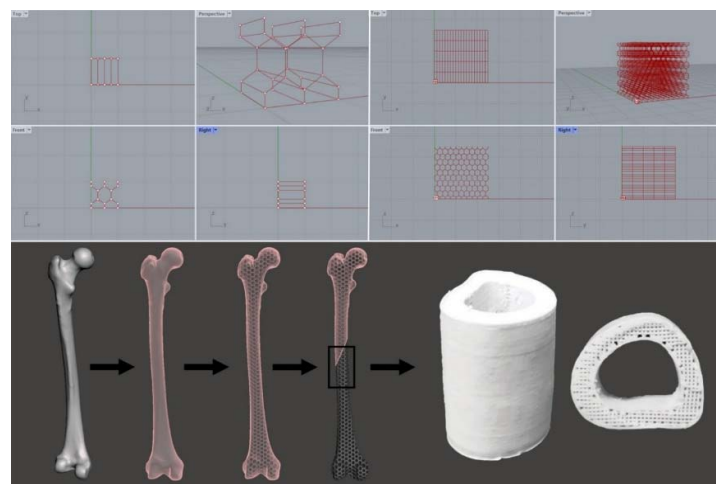


Fig. 2. Parametric design steps of a honeycomb structure from the elementary cell used as infill pattern in the final printed scaffold.

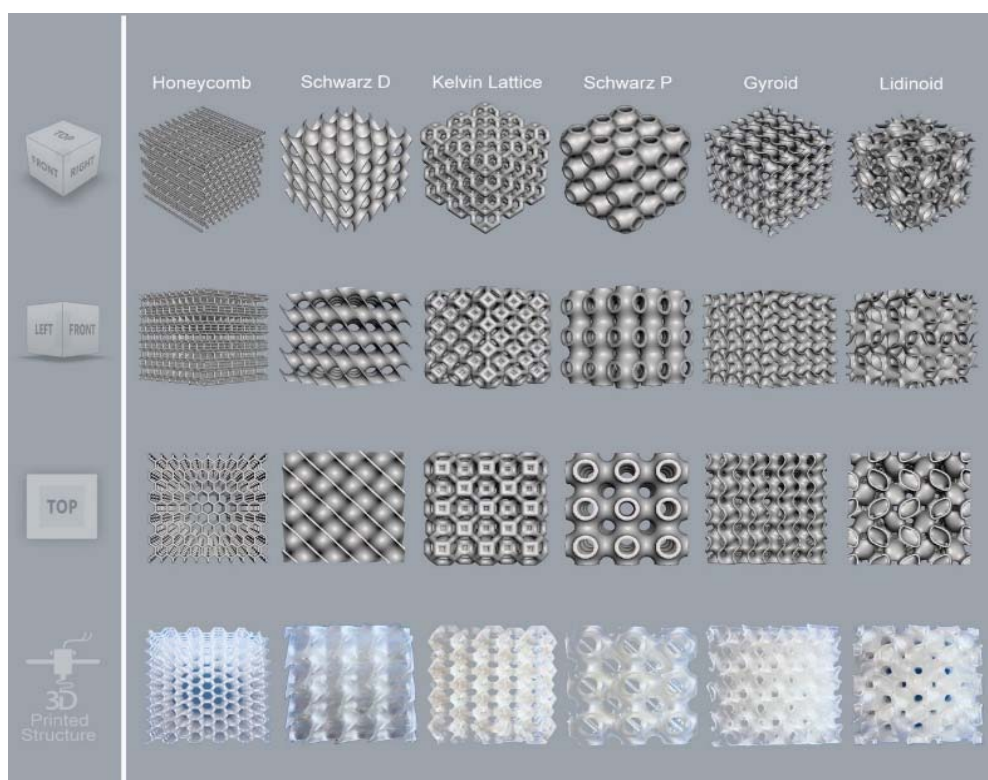


Fig. 3. Designed triply periodic minimal surfaces and functionally graded lattice structures. Modeled based on various cell geometries using Rhino 7 and the final printed models.

As the primary goal was to investigate the effect of design variation on the mechanical properties and the geometrical scaffold requirements, such as pore interconnectivity does not depend on the scaffold scale, all scaffolds were designed as cubes with dimensions of 20 mm (Fig. 3).

### 2.3. Scaffolds printing

3D printing of models was done by an inexpensive SLA 3D printer (Anycubic Photon S). The UV-cured resin was used as scaffold matrix due to features such as biodegradability, low cost, ease of manufacture, tunable mechanical properties, adequate viscosity, and ease of use in 3D printing [22–24]. The resin properties are presented in Table 1.

Physico-chemical parameters of all six structures are shown in Table 2.

The viscosity of the UV-cured resin was measured using a viscometer (TMAX NDJ-8S, China) at temperatures of 25 to 50 °C and rotation speeds of 6 to 60 rpm, respectively.

### 2.4. Finite element analysis

Obtained data were processed and analyzed using the JMP Pro 16 software. Compression and tensile tests were simulated in Abaqus/CAE 2020 according to ASTM D695 and ASTM D638 standards. Six structures with the best performance in simulations compared to others were selected as primary scaffolds. FEA (Quasi-Static) analysis

**Table 1**  
Physico-chemical properties of biodegradable resin

Hardness	84D	Bending strength	59-70 MPa
Viscosity	150-300 MPa·s	Extension strength	36-52 MPa
Shrinkage	3.72-4.24%	Vitrification temperature	100 °C
Shelf time	1 year	Thermal deformation	80 °C
Solid density	1.05-1.25 g/cm <sup>3</sup>	Elongation at break	11-20%
Wave length	355-410 nm	Viscosity	592.0 mPa·s

**Table 2**  
Scaffold parameters – Specimens that contain hydroxyapatite and calcium pyrophosphate are marked with (\*)

	Honeycomb	Schwarz minimal surfaces (Schwarz D)	Weaire-Phelan structure (Kelvin Lattice)	Schwarz minimal surfaces (Schwarz P)	Alan Schoen's Gyroid	Sven Lidin's Lidinoid
Weight (gr)	1.1-1.18*	1.4-1.48*	2.1-2.26*	1.9-2.05*	1.8-1.93*	1.6-1.71*
Dimension (mm)	20.20.20	20.20.20	20.20.20	20.20.20	20.20.20	20.20.20
Mass fraction (HA/ Calcium pyrophosphate/Resin)*	10.05-0.05-0.9*	10.05-0.05-0.9*	10.05-0.05-0.9*	10.05-0.05-0.9*	10.05-0.05-0.9*	10.05-0.05-0.9*
Average Pore Size	300-400 $\mu\text{m}$	400-700 $\mu\text{m}$	400-500 $\mu\text{m}$	500-800 $\mu\text{m}$	300-400 $\mu\text{m}$	300-400 $\mu\text{m}$
Shore hardness	84D	84D	84D	84D	84D	84D
Shrinkage percent	3.72-4.24%	3.72-4.24%	3.72-4.24%	3.72-4.24%	3.72-4.24%	3.72-4.24%
Vitrification temperature	100 $^{\circ}\text{C}$					
Thermal deformation temperature	80 $^{\circ}\text{C}$ 78 $^{\circ}\text{C}^*$					
Elongation at break	3.41%-3.24%*	2.87%-2.77%*	2.73%-2.61%*	3.41%-3.33%*	4.26%-4.11%*	3.93%-3.81%*
Porosity (%)	76.23	72.26	71.14	68.62	66.11	64.28

of the Kelvin lattice structure as infill pattern in 3 specific cuts of the femur bone is presented in Fig. 7.

### 2.5. Tensile and compression tests

The universal testing system (Metrotest REM-50) was utilized for printed scaffold compression and tensile tests.

## 3. Results and discussion

### 3.1. Characterization of HA and CPP powders

XRD analysis (Fig. 4) showed that HA and CPP powders are pure (more than 95%). The average crystallite size of the HA and CPP powders was evaluated from the peak broadening of the XRD patterns based on Scherrer's equation which was 2.21  $\mu\text{m}$  for HA and 3.11  $\mu\text{m}$  for CPP. The FESEM images show that the powders are in optimum condition with minimum agglomeration compared to available commercial powders (Sigma-Aldrich CAS no. 1306-06-5). As shown in the graph, some impurities such as Calcium phosphate ( $\text{Ca}_3(\text{PO}_4)_2$ ) and Calcium oxide (CaO) existed in HA powder after heat treatment which can be due to the higher decomposition temperature than hydroxyapatite and undesirable Calcium metaphosphate ( $\text{CaP}_2\text{O}_6$ )

in CPP powder can appear during transformation which can be ignored due to its small amount.

#### 3.1.1. Resin composite

To make the composite, HA/ CPP were used as precursors. 5 wt.% of HA/ CPP were mixed with pure resin, and 1 h sonicating and mechanical dispersion were done. The composite was placed at rest for 1 h to remove formed bubbles in the degassing stage. Derivative thermogravimetry and thermogravimetric analysis were carried out.

The resin viscosity has a significant impact on the 3D printing process. Objects' deformation can occur due to the high viscosity. The decrease in viscosity is observed with increasing temperature (Fig. 5(A)), and after the temperature exceeded 37  $^{\circ}\text{C}$ , it almost reached a plateau. The addition of 5 wt.% HA/ CPP increases the viscosity of the resin. At room temperature, the viscosity of the liquid resin which contains or does not contain HA/ CPP was 0.839 Pa.s and 0.501 Pa.s, respectively, which is appropriate for stereolithography.

Figure 5B shows the thermal stability test of resin in temperatures ranging from 30 to 500  $^{\circ}\text{C}$  and  $\text{N}_2$  atmosphere. Below 200  $^{\circ}\text{C}$ , it was thermally stable, but due to fragmentation of the macromolecules, dismutation, and gasification processes, a quick weight loss was observed at 260  $^{\circ}\text{C}$ .

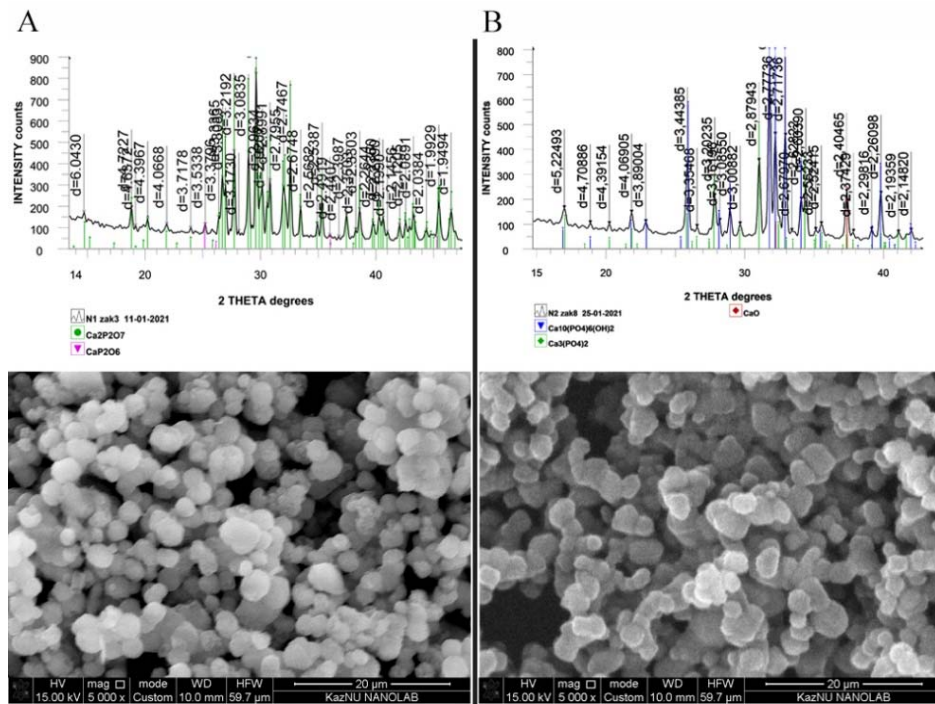


Fig. 4. XRD pattern and FESEM images of samples after heat treatment and grinding: A – Calcium Pyrophosphate; B – Hydroxyapatite.

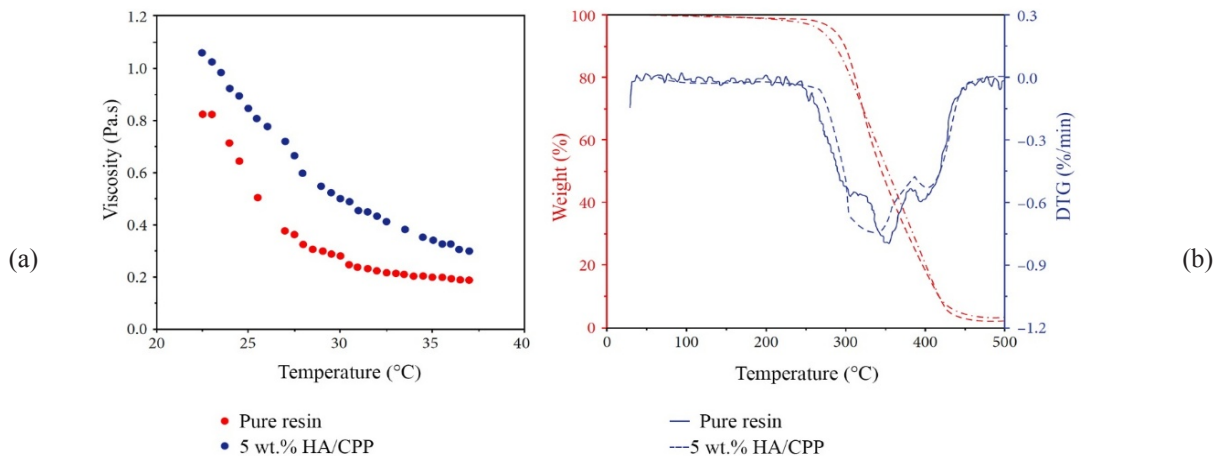


Fig. 5. A) The viscosities of pure resin compare to the resin which contains HA/CPP at various temperatures. B) TGA and DTG curves of pure resin compare to the resin which contains HA/CPP.

By increasing temperature above 440 °C, the resin weight remained constant, which indicates that decomposition is complete. The degradation temperature of HA/CPP resin composite is higher than resin reference, meaning that adding HA/CPP to UV cured resin could improve its thermal stability.

### 3.2. Printed scaffolds mechanical properties

#### 3.2.1. Compression strength

Two groups of scaffolds were printed. In the

first group, six scaffolds were printed using biodegradable resin made from soybean oil as the matrix (made by Anycubic Co.). In the second group, six scaffolds were printed using a mixture of biodegradable UV-cured resin with 5% W/W of hydroxyapatite and 5% W/W calcium pyrophosphate. The compression test was performed on both groups, and results are presented in the Table 3.

Results show the reduction in compression resistance by adding the resin precursor, and Kelvin lattice has been the most robust structure. Figure 6 shows the compression test steps on Schwarz P structure as an example.

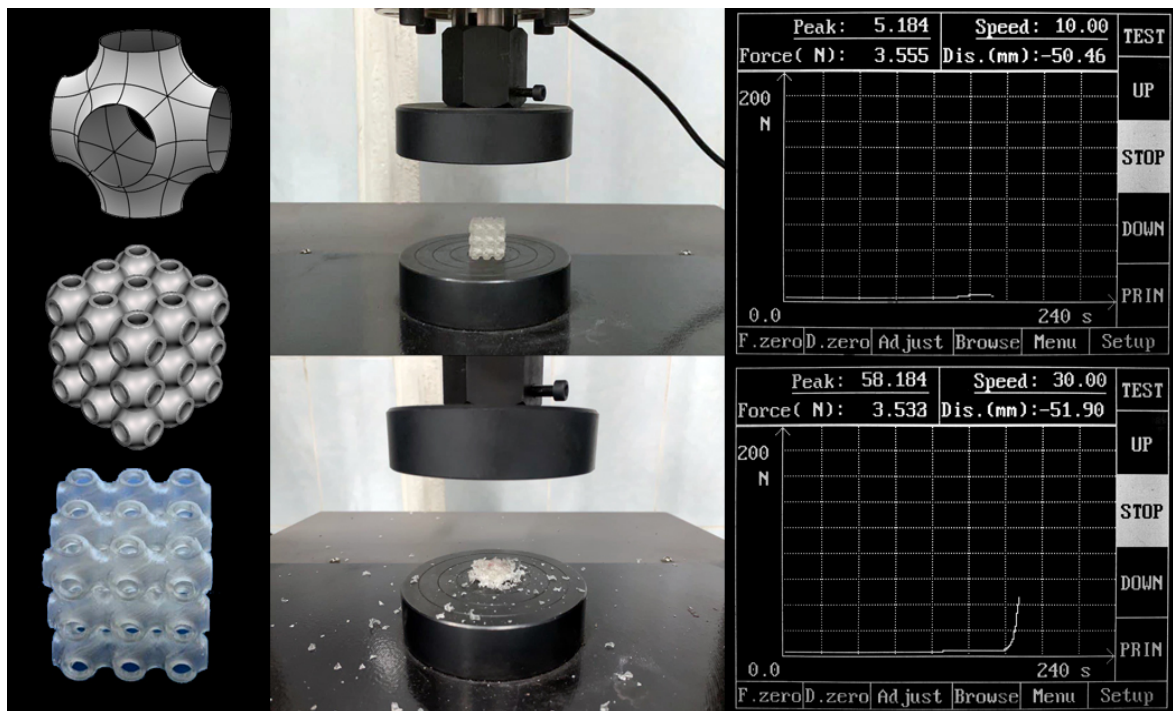


Fig. 6. Compression test on Schwarz P structure done by universal testing system.

**Table 3**

Compression test result for each structure – structures that contain hydroxyapatite and calcium pyrophosphate are marked with (\*)

Structure	Initial Crack (N)	Full Destruction (N)
Schwarz P	5.184-5.098*	58.184-57.211*
Schwarz D	4.751-4.437*	58.918-57.852*
Honeycomb	4.074-3.909*	58.312-57.714*
Gyroid	4.451-4.152*	57.544-56.709*
Kelvin Lattice	6.029-5.898*	58.240-57.606*
Lidinoid	4.933-4.533*	53.344-52.018*

### 3.2.2. Tensile strength

Before tensile testing, the 3D printed specimens must be conditioned according to ASTM D638 standards. For 40 h, 3D printed specimens are conditioned at 230 °C. Conditioning them alters the molecular structure of the plastic, which improves their properties.

The standard specimen's inside was printed with 100% infill without any specific orientations. Tensile testing of the specimens was conducted on Metrotest REM-50 with a 25 kN load cell. All tests were conducted at 20–25 °C. Built-in linear variable differential transformers (LVDT) were used to measure displacement. Six specimens were tested with different structures. Table 4 present the individual test results for each specimen.

Modulus of Elasticity (=Young modulus in tension) was determined using the following formula [25]:

$$E = \frac{\sigma}{\varepsilon} = \delta = \frac{\text{Stress}}{\text{Strain}}$$

where E is Young's modulus;  $\sigma$  is Tensile stress;  $\varepsilon$  is Axial strain;  $\delta$  is Elastic modulus.

Tensile stress and strain can be obtained using the following equations [25]:

$$\sigma = \frac{F}{A} ; \quad \varepsilon = \frac{\Delta L}{L}$$

where F is the tensile force applied, A is the cross-sectional area of the specimen,  $\Delta L$  is the change in length in the loading direction, and L is the original length of the specimen.

The experimental results were in good agreement with the simulations. They confirmed the decrease in specific ultimate tensile strength as the infill percentage decreases, and in particular, the Gyroid structure was more robust than others. There is a direct relationship between porosity and tensile strength, and with increasing porosity, tensile strength decreases.

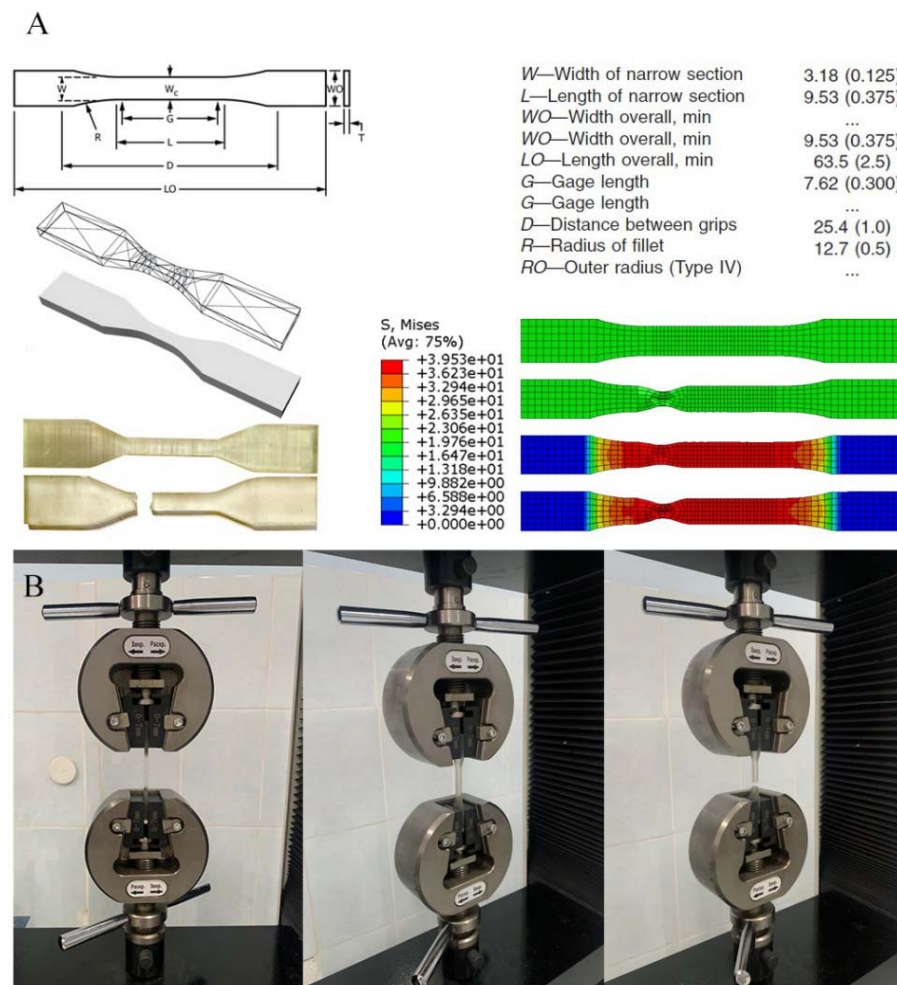


Fig. 7. A) Design parameters and tensile simulation results in Abaqus/CAE 2020 according to ASTM D638 standard. B) Tensile tests of a standard specimen using the universal testing system.

**Table 4**  
Individual Tensile test results for each specimen. Specimens that contain hydroxyapatite and calcium pyrophosphate are marked with (\*)

Specimen structure	Precise width (mm)	Precise thickness (mm)	Ultimate stress (MPa)	Elongation at break (%)	Modulus of elasticity (GPa)
Honeycomb	9.56-9.54*	3.19-3.20*	56.62-55.94*	2.31%-2.16%*	3.15-3.09*
Schwarz D	9.54-9.55*	3.20-3.19*	59.68-58.71*	2.19%-2.09%*	3.11-3.07*
Kelvin Lattice	9.58-9.55*	3.20-3.20*	59.12-58.91*	1.66%-1.57%*	3.13-3.10*
Schwarz P	9.56-9.54*	3.21-3.19*	58.71-58.01*	2.11%-2.01%*	3.21-3.16*
Gyroid	9.53-9.54*	3.19-3.21*	60.12-59.57*	1.74%-1.65%*	3.19-3.13*
Lidinoid	9.54-9.53*	3.21-3.19*	60.06-59.32*	2.01%-1.89%*	3.17-3.11*

### 3.3. Finite element analysis

Abaqus FEA software was used to design scaffolds with variable cell geometries to achieve various porosity and permeability levels and investigate their geometric and mechanical requirements for orthopedic uses.

In the simulations performed on the elasticity and strength of the specimens in Abaqus software, we used the proposed micromechanical model presented by Fritsch et al. [26] to predict the mechanical behavior of hydroxyapatite biomaterials to bring the results as close to reality as possible. In addition, the method presented by D. Nguyen

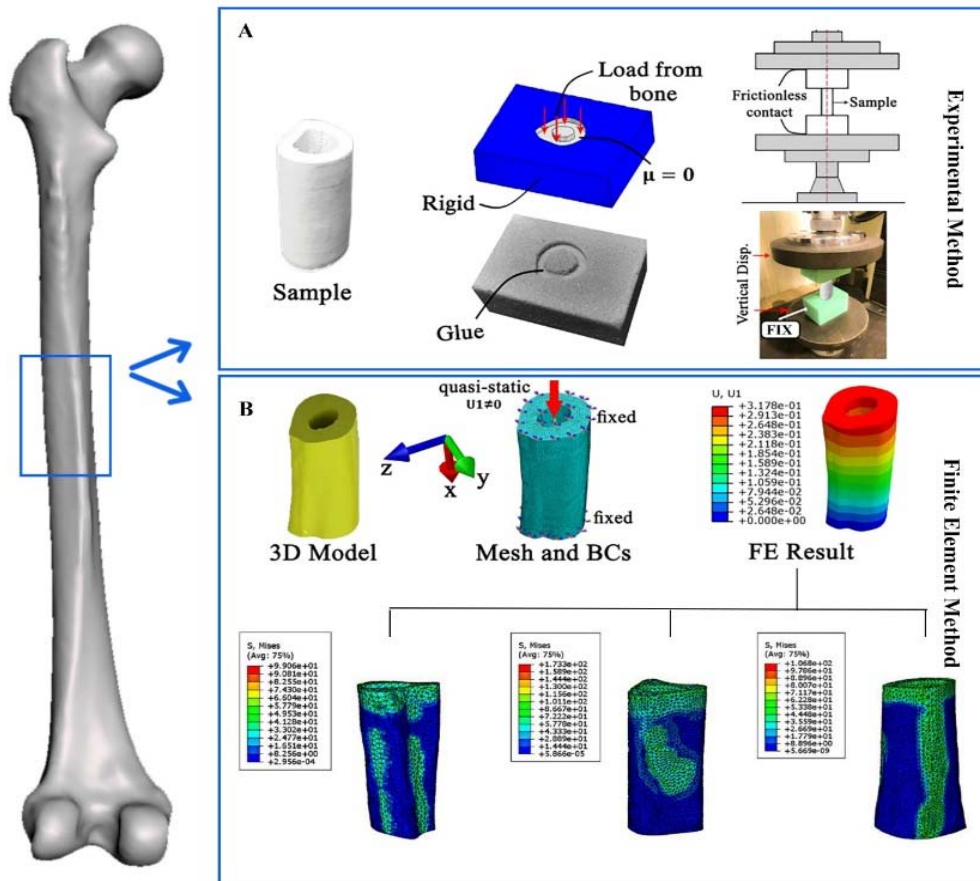


Fig. 8. A) Setup for compression test of a 3D printed femur bone (4 cm length, 2.7 cm diameter). B) Quasi-static analyzing of the Kelvin Lattice structure as infill pattern in 3 specific cuts of the femur bone.

et al. [27] was used to investigate the mechanical properties of lattice structures. Figure 8 shows the Quasi-Static Analysing of the Kelvin Lattice structure as an infill pattern which is in good agreement with the experimental result.

#### 4. Conclusion

According to the obtained results, it is inferred that by adding precursor (CPP, HA) to the matrix, the mechanical strength of scaffolds decreases. Kelvin lattice and gyroid are the best structures that show more resistance against the different loading and tensile forces. Both structures' high porosity and low weight make them an ideal candidate for orthopedic surgery. Finite Element Analysis results were in good agreement with the obtained experimental result of the Gyroid, Kelvin lattice, and Schwarz P structures. The only exception was the Honeycomb structure, where both the tensile and loading resistance values in the experiment were significantly lower than the FEA results.

To perform the FEA, the base material was tested under tensile and compressive loading conditions where different strain rates were applied, and the findings were used to calibrate the Arruda-Boyce model. The tensile test found that the percent elongation reduces as the slimness ratio rises and the cross-sectional area decreases. Stress concentration effects are minimized because there are no joints or discontinuities in TPMS constructions.

The effect of HA and CPP on the mechanical strength of scaffolds versus their positive impact on bone regeneration is minimal, and HA/ CPP can be used as an ideal agent in bioscaffolds.

#### Acknowledgment

The authors would like to thank the Institute of combustion problems (Almaty, Kazakhstan) for laboratory facilities and cooperation to execute this study.

## References

- [1]. U. Jammalamadaka, K. Tappa, *J. Funct. Biomater.* 9 (2018) 22. DOI: [10.3390/jfb9010022](https://doi.org/10.3390/jfb9010022)
- [2]. A.-V. Do, B. Khorsand, S.M. Geary, A.K. Salem, *Adv. Healthc. Mater.* 4 (2015) 1742–1762. DOI: [10.1002/adhm.201500168](https://doi.org/10.1002/adhm.201500168)
- [3]. A.A.M. Shimojo, I.C.P. Rodrigues, A.G.M. Perez, E.M.B. Souto, L.P. Gabriel, T. Webster (2020) Scaffolds for Tissue Engineering: A State-of-the-Art Review Concerning Types, Properties, Materials, Processing, and Characterization. In: Li B., Moriarty T., Webster T., Xing M. (eds) *Racing for the Surface*. Springer, Cham. DOI: [10.1007/978-3-030-34471-9\\_23](https://doi.org/10.1007/978-3-030-34471-9_23)
- [4]. J.J. Chung, H. Im, S.H. Kim, J.W. Park, Y. Jung, *Front. Bioeng. Biotechnol.* 8 (2020). DOI: [10.3389/fbioe.2020.586406](https://doi.org/10.3389/fbioe.2020.586406)
- [5]. K. Wang, X. Xie, J. Wang, A. Zhao, Y. Peng, Y. Rao, *Results Phys.* 18 (2020) 103346. DOI: [10.1016/j.rinp.2020.103346](https://doi.org/10.1016/j.rinp.2020.103346)
- [6]. Q. Ma, M.R.M. Rejab, A.P. Kumar, H. Fu, N.M. Kumar, J. Tang, *Proc. Inst. Mech. Eng. Part C J. Mech. Eng. Sci.* 235 (2020) 4254–4272. DOI: [10.1177/0954406220971667](https://doi.org/10.1177/0954406220971667)
- [7]. M. Bahraminasab, K.L. Edwards, (2019) Computational Tailoring of Orthopaedic Biomaterials: Design Principles and Aiding Tools. In: Bains P., Sidhu S., Bahraminasab M., Prakash C. (eds) *Biomaterials in Orthopaedics and Bone Regeneration*. Materials Horizons: From Nature to Nanomaterials. Springer, Singapore. DOI: [10.1007/978-981-13-9977-0\\_2](https://doi.org/10.1007/978-981-13-9977-0_2)
- [8]. H. Lin, D. Zhang, P.G. Alexander, G. Yang, J. Tan, A.W.-M. Cheng, R.S. Tuan, *Biomaterials* 34 (2013) 331–339. DOI: [10.1016/j.biomaterials.2012.09.048](https://doi.org/10.1016/j.biomaterials.2012.09.048)
- [9]. G. Noussios, K. Theologou, P. Chouridis, G. Karavasilis, G. Alafostergios, A. Katsourakis, *J. Clin. Med. Res.* 11 (20119) 740–744. DOI: [10.14740/jocmr3986](https://doi.org/10.14740/jocmr3986)
- [10]. S. Terekhina, I. Skorniyakov, T. Tarasova, S. Egorov, *Technologies* 7 (2019) 57. DOI: [10.3390/technologies7030057](https://doi.org/10.3390/technologies7030057)
- [11]. H. Sharda, A. Kumar, A View on Why Infill Ratio and Infill Type is the Backbone of the Strength of 3D Printing Models in Affordable Printing, *International Journal for Scientific Research and Development* 7 (2019) 589–591.
- [12]. A. Chapman, E. Naseri, S. Wheatley, R.A. Tasker, A. Ahmadi, *Progress in Canadian Mechanical Engineering* 3 (2020). DOI: [10.32393/csme.2020.1288](https://doi.org/10.32393/csme.2020.1288)
- [13]. S.V. Murphy, A. Atala, *Nat. Biotechnol.* 32 (2014) 773–785. DOI: [10.1038/nbt.2958](https://doi.org/10.1038/nbt.2958)
- [14]. K. Byrappa, M. Yoshimura, *History of Hydrothermal Technology*. Handbook of Hydrothermal Technology (2 Ed.) 2013, p. 51–73. DOI: [10.1016/B978-0-12-375090-7.00002-5](https://doi.org/10.1016/B978-0-12-375090-7.00002-5)
- [15]. F. Ahmed, A. Azam, M.M. Khan, S.M. Mugo, *J. Nanomater.* 2018, Article ID 3692420. DOI: [10.1155/2018/3692420](https://doi.org/10.1155/2018/3692420)
- [16]. Z.A. Mansurov, *Eurasian Chem.-Technol. J.* 22 (2020) 241–253. DOI: [10.18321/ectj994](https://doi.org/10.18321/ectj994)
- [17]. C. Daulbayev, Z. Mansurov, F. Sultanov, M. Shams, A. Umirzakov, S. Serovajsky, *Eurasian Chem.-Technol. J.* 22 (2020) 149–156. DOI: [10.18321/ectj974](https://doi.org/10.18321/ectj974)
- [18]. C. Daulbayev, F. Sultanov, B. Bakbolat, O. Daulbayev, *Int. J. Hydrogen Energy* 45 (2020) 33325–33342. DOI: [10.1016/j.ijhydene.2020.09.101](https://doi.org/10.1016/j.ijhydene.2020.09.101)
- [19]. T.H.A. Corrêa, J.N.F. Holanda, *Ceramica* 62 (2016) 278–280. DOI: [10.1590/0366-69132016623631986](https://doi.org/10.1590/0366-69132016623631986)
- [20]. C. Daulbayev, F. Sultanov, M. Aldasheva, A. Abdybekova, B. Bakbolat, M. Shams, A. Chekiyeva, Z. Mansurov, *Comptes Rendus. Chim.* 24 (2021) 1–9. DOI: [10.5802/crchim.58](https://doi.org/10.5802/crchim.58)
- [21]. S.C. Wu, H.C. Hsu, S.K. Hsu, Y.C. Chang, W.F. Ho, *Ceram. Int.* 41 (2015) 10718–10724. DOI: [10.1016/j.ceramint.2015.05.006](https://doi.org/10.1016/j.ceramint.2015.05.006)
- [22]. R. Pugliese, B. Beltrami, S. Regondi, C. Lunetta, *Annals of 3D Printed Medicine* 2 (2021) 100011. DOI: [10.1016/j.stlm.2021.100011](https://doi.org/10.1016/j.stlm.2021.100011)
- [23]. J.W. Stansbury, M.J. Idacavage, *Dent. Mater.* 32 (2016) 54–64. DOI: [10.1016/j.dental.2015.09.018](https://doi.org/10.1016/j.dental.2015.09.018)
- [24]. S.C. Ligon, R. Liska, J. Stampfl, M. Gurr, R. Mülhaupt, *Chem. Rev.* 117 (2017) 10212–10290. DOI: [10.1021/acs.chemrev.7b00074](https://doi.org/10.1021/acs.chemrev.7b00074)
- [25]. H. Czichos, T. Saito, L.E. Smith, Springer Handbook of Materials Measurement Methods, Springer Handb. Mater. Meas. Methods, 2006, DOI: [10.1007/978-3-540-30300-8](https://doi.org/10.1007/978-3-540-30300-8)
- [26]. A. Fritsch, L. Dormieux, C. Hellmich, J. Sanahuja, *J. Biomed. Mater. Res. Part A* 88 (2009) 149–161. DOI: [10.1002/jbm.a.31727](https://doi.org/10.1002/jbm.a.31727)
- [27]. D.S. Nguyen, T.A. Nguyen-Van, *J. Korean Soc. Precis. Eng.* 37 (2020) 305–318. DOI: [10.7736/JKSPE.019.100](https://doi.org/10.7736/JKSPE.019.100)